J. Fluid Mech. (1981), *vol.* 105, *pp.* 61–85
Printed in Great Britain

Bubbles in viscous liquids: shapes, wakes and velocities

By D. BHAGA† AND M. E. WEBER
Department of Chemical Engineering, McGill University, Montreal, P.Q., Canada

(Received 4 June 1979 and in revised form 12 August 1980)

The shapes and terminal velocities of bubbles rising in viscous liquids have been determined. For Morton numbers (M) greater than 4×10^{-3} the drag coefficient and dimensionless bubble shape are functions only of Reynolds number (R). Shape regimes and terminal rise velocities have been correlated. The flow field around a rising bubble was visualized through the hydrogen bubble tracer technique. For $M > 4 \times 10^{-3}$ and $R < 110$ the bubbles trailed closed, laminar toroidal wakes. For $R > 110$ the wake was open and unsteady. Streamlines for the flow were obtained by raising a ciné camera at the same speed as the bubble and filming the H_2 tracer bubbles. Results are presented for $R < 150$ and $7{\cdot}4 \times 10^{-4} < M < 850$.

1. Introduction

Single bubbles rising in liquids have been studied for a number of years. Aside from the terminal rise velocity we know little about the flow field around a bubble. At very low Reynolds numbers the theoretical development of Taylor & Acrivos (1964) provides a description of the shape of a bubble and the velocity field around it. At higher Reynolds numbers only boundary-layer approximations (Moore 1963; Harper & Moore 1968; Parlange 1970) and semi-empirical models (Parlange 1969) are available. All assume unrealistic shapes for the bubble. Harper (1972) and Clift, Grace & Weber (1978) provide good summaries of present knowledge.

In this paper we present experimental data and correlations of bubble rise velocity and shape in §§3 and 4. The nature and geometry of the wake are reported in §5. Streamlines of the flow around a rising bubble obtained by the hydrogen tracer-bubble technique are presented for a wide range of Reynolds numbers in §6. Section 7 compares some of the present data with the few models available for the flow.

The experimental results are presented in terms of the following dimensionless groups (see Grace 1973; Clift *et al.* 1978):

$$\text{Reynolds number,} \quad R = \frac{\rho d_e U}{\mu}; \tag{1}$$

$$\text{Eötvös number,} \quad E = \frac{g d_e^2 \rho}{\sigma}; \tag{2}$$

$$\text{Morton number,} \quad M = \frac{g\mu^4}{\rho\sigma^3}. \tag{3}$$

The commonly used drag coefficient and Weber number are not independent of this set:

$$\text{drag coefficient,} \quad C_D = \frac{4gd_e}{3U^2} = \frac{4E^{\frac{3}{2}}}{3R^2M^{\frac{1}{2}}}; \tag{4}$$

† Present address: Chemetics International, Toronto, Ontario.

$$\text{Weber number,} \quad W = \frac{\rho U^2 d_e}{\sigma} = \frac{R^2 M^{\frac{1}{2}}}{E^{\frac{1}{2}}}. \tag{5}$$

The characteristic length, $d_e = (6V/\pi)^{\frac{1}{3}}$, is the volume-equivalent diameter of a bubble of volume V and U is its terminal rise velocity; ρ, μ and σ are, respectively, the density, viscosity and surface tension of the liquid and g is the acceleration of gravity.

Harper (1972) makes a distinction between high- and low-Morton-number liquids. He characterizes the high-M liquids as those in which C_D decreases monotonically with R while for the low-M liquids the C_D–R curve has a minimum. This minimum reflects a local maximum in the terminal rise velocity/bubble volume relationship. Although the value of M separating the high and low M liquids is not known precisely, see Harper (1972), our data place it at $M \doteq 4 \times 10^{-3}$. Most of the data reported here are for high-Morton-number liquids, i.e. for M above this value.

2. Experimental apparatus

The basic technique consisted of photographing a rising bubble with a ciné camera moving upward at the same speed as the bubble. The rate of ascent of the camera could be varied. The camera elevator speed was set equal to the subject bubble speed from earlier calibration runs. Using this technique the bubble remained in the centre of the frames in the ciné film throughout its rise.

The velocity field around the rising bubble was visualized by hydrogen bubbles introduced electrolytically into the liquid. Lighting was principally from the side through a slit to illuminate the tracer bubbles by a thin sheet of light. Some auxiliary backlighting was also used to outline the subject bubble.

The experimental set-up is shown schematically in figure 1. The test liquids, aqueous sugar solutions of differing concentrations, were held in a Plexiglas column (1) 183 cm height, 29·2 cm inside diameter and 0·6 cm wall thickness. To reduce optical distortion a square Plexiglas box (2) of 1 cm wall thickness and 38 × 38 cm cross-section was placed around the upper 122 cm of the column. The space between the square and cylindrical column was also filled with the test liquid. The bubbles were introduced from a hemispherical dumping cup (3) of 7·6 cm inside diameter. A known volume of air was supplied to the cup from a calibrated syringe. An inverted glass funnel (5) placed above the cup centred the bubble in the column. After release the bubble rose to interrupt the light beam at the lower photocell (7) which activated the clock (9), the pulse generator (11) and the camera-moving device (14). When the bubble passed the upper photocell these instruments were switched off. The pulse generator triggered high voltage (up to 750 volts) pulses of electricity to the cathode (13) where the hydrogen tracer bubbles were generated.

The H_2 tracer technique has been used for a number of years in water flows, see Schraub *et al.* (1965). To use it successfully in aqueous sugar solutions required only the provision of high voltage pulses. A more serious problem was posed by the introduction of the tracer bubbles into the closed, toroidal wake which was carried with most of the subject bubbles in this study. The cathode was a 0·025 cm tungsten wire which extended radially from the wall to near the centre of the column. The wire was alternately insulated and left bare in 0·2 cm lengths. The bubble passing over this wire was not broken and H_2 tracer bubbles were introduced into the wake by activa-

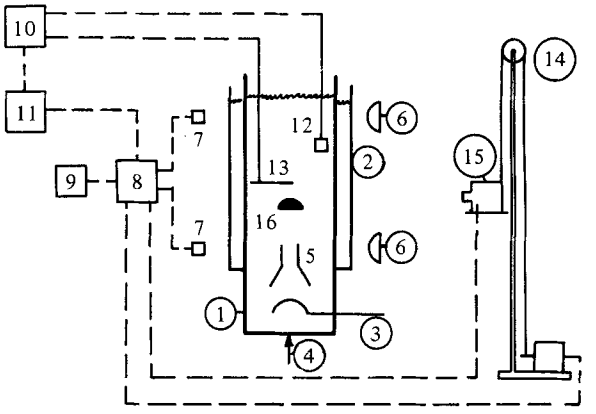

FIGURE 1. Schematic diagram of apparatus: 1, test column; 2, square box; 3, dumping cup; 4, air inlet; 5, inverted funnel; 6, flashlights; 7, photocells; 8, relay unit; 9, clock; 10, d.c. power supply; 11, pulse generator; 12, wire anode; 13, cathode; 14, camera-raising device; 15, 16 mm ciné camera; 16, rising bubble.

tion of the pulse generator as described above. The cathode was positioned along the column radius in such a way that it extended 2 mm beyond the column axis, thus covering slightly more than half of the column. Cathode wires which spanned the column broke the subject bubble.

The H_2 tracer bubbles were illuminated by a collimated sheet of light 2–3 mm thick spanning the column diameter. Filming was with a 16 mm Bolex ciné camera and 400ASA reversal film at speeds between 12 and 40 frames per second. Measured tracer bubble rise velocities in the stagnant liquids were between 0·013 and 0·018 cm s^{-1} while subject bubble rise velocities were at least two and usually three orders of magnitude larger.

Measurements of the bubble outline and the positions of the tracer bubbles were made from frame-by-frame projections of the ciné film on a semi-transparent screen. Magnifications were obtained from an accurate scale which was suspended in the liquid and photographed in the first few frames of each film. Optical distortion was less than 1 %. Bubble shapes were well approximated by segments of ellipsoids or spheres. For ellipsoidal bubbles the values of the major and minor semi-axes, a and b, were obtained by taking the co-ordinates of 5 pairs of points on the tracing of the bubble surface and then calculating 5 values of a and b from the equation describing an ellipse. The values of a and b for each bubble were determined by averaging these 5 values. Repetitive calculations gave errors in these parameters of less than 7 %. For spherical bubbles ($a/b > 0{\cdot}95$) the frontal radius was obtained by superimposing over the tracing a clear plastic plate on which circles of different radii were drawn. Accuracy of better than 5 % was obtained.

The tracer bubbles were filmed at several framing rates. At the lowest framing rate, 12 frames per second, the tracer bubbles appeared as streaks, giving a good visual impression of the flow field. Higher framing rates were used in the determination of streamlines and velocities so that the tracers appeared as bright spots and could be followed individually from frame to frame. The tracer paths were traced directly from the projected film. Velocities were calculated by dividing the distance travelled by a tracer bubble in two adjacent frames by the time elapsed.

(a)

(b)

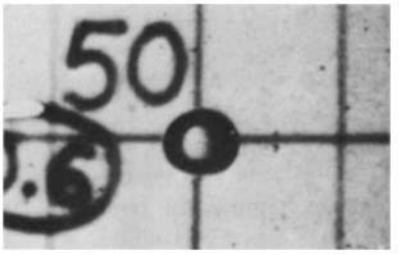

(c)

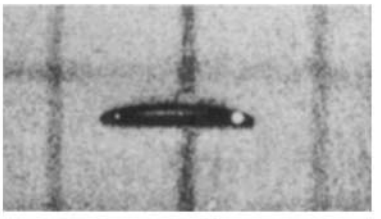

(d)

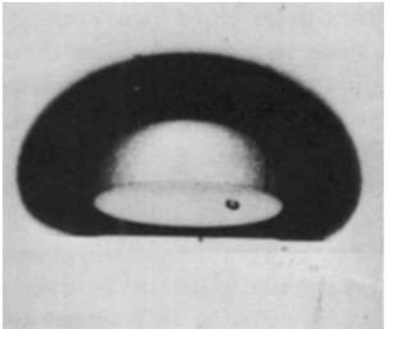

(e)

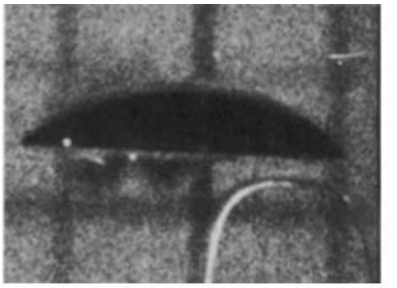

(f)

(g)

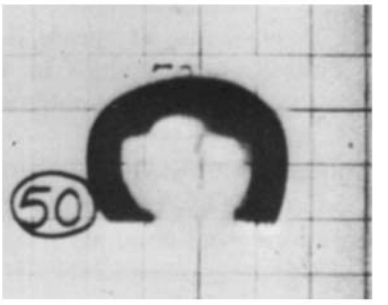

(h)

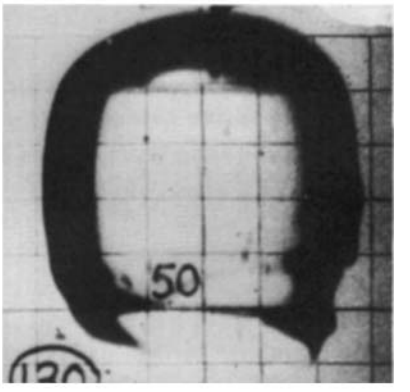

Fluid density, viscosity and surface tension were measured by standard methods. The viscosity of the solution is the physical property most sensitive to concentration for the aqueous sugar solutions used here. We used viscosities from 0·82 to 28·0 poise. Over this range the density varied from only 1·314 to 1·390 g cm^{-3} and the surface tension from only 76·9 to 80·0 dynes cm^{-1}. The corresponding variation in the Morton number, M, was from $7{\cdot}4 \times 10^{-4}$ to 850.

In all cases the air bubbles were injected only after liquid motion from earlier bubbles had ceased. Bubble volumes were corrected to the hydrostatic pressure at the location of measurement. Replicate runs showed excellent reproducibility for both the terminal rise velocity and for the tracer trajectories. Additional details are available (Bhaga 1976).

3. Bubble shape

Figure 2 shows photographs of air bubbles in aqueous sugar solutions. The shapes were classified as spherical, oblate ellipsoidal, oblate ellipsoidal cap, spherical cap with open or closed wake and skirted bubbles with smooth or wavy skirts.† The disk-like bubble shown in (*c*) was found for $40 < R < 70$ in the least viscous solution. These bubbles wobbled as they rose although both larger and smaller bubbles in the same solution rose rectilinearly. Figure 3 shows the effect of viscosity (or M) on bubble shape for a bubble of 9·3 cm^3 volume. All bubbles are shown at the same magnification. At low R the bubble is nearly a complete oblate spheroid. With decreasing viscosity and increasing R it becomes a smaller segment of an oblate spheroid. It is a half spheroid for $R \doteq 25$. At $R \doteq 45$ a spherical cap shape is found. For all R except the highest in figure 3 the wake is closed; for the highest R the wake is open and the base of the bubble oscillates as illustrated in the final photograph.

The shapes are characterized either by segments of oblate ellipsoids or by segments of spheres as shown in figure 4. The parameters defining the shape are functions only of R for high-M liquids as shown in figures 5 and 6. This is in contrast to the results for low-viscosity liquids where the shape is a function of both R and M, see Tadaki & Maeda (1961). Figure 6 shows the aspect ratio of the ellipsoid forming the front part of the bubble. At low R the bubbles deform from spheres to oblate spheroids and then to spherical cap shape at $R > 45$. At $R < 0{\cdot}5$, $W < 1$ the bubble shape agrees with the predictions of Taylor & Acrivos (1964). The aspect ratio of the bubble, h/w, and the included angle, θ, decrease toward constant values at high R as found by many

† The skirts trailed behind bubbles are extremely thin, of the order of 100 μm, see Guthrie & Bradshaw (1969). The difference in refractive index between the gas and the liquid makes them appear much thicker in the photographs.

FIGURE 2. Typical bubbles (grid in background is 2 × 2 cm).

	E	M	R	Shape
(*a*)	8·67	711	0·078	spherical
(*b*)	17·7	711	0·232	oblate ellipsoidal
(*c*)	32·2	$8{\cdot}20 \times 10^{-4}$	55·3	oblate ellipsoidal (disk)
(*d*)	243	266	7·77	oblate ellipsoidal cap
(*e*)	115	$4{\cdot}63 \times 10^{-3}$	94·0	spherical cap (closed wake)
(*f*)	237	$8{\cdot}20 \times 10^{-4}$	259	spherical cap (open wake)
(*g*)	339	43·1	18·3	skirted (smooth)
(*h*)	641	43·1	30·3	skirted (wavy)

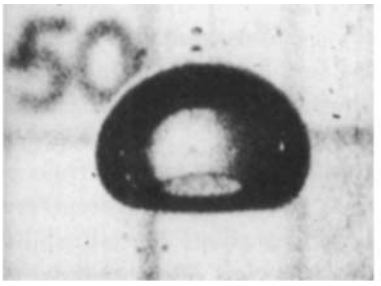
(a)

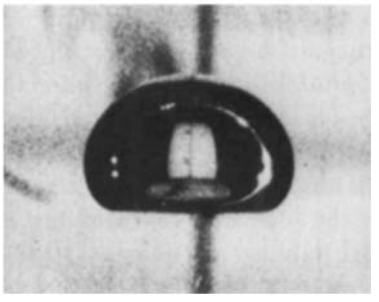
(b)

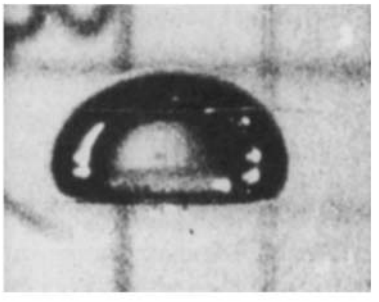
(c)

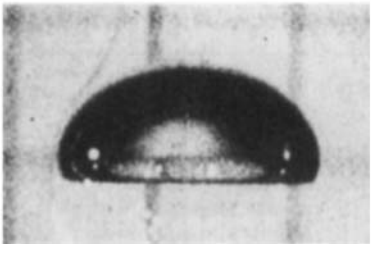
(d)

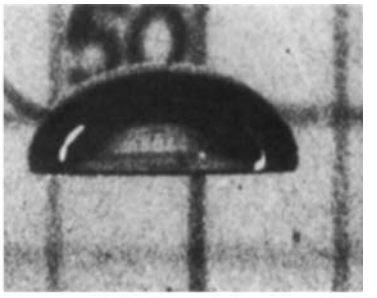
(e)

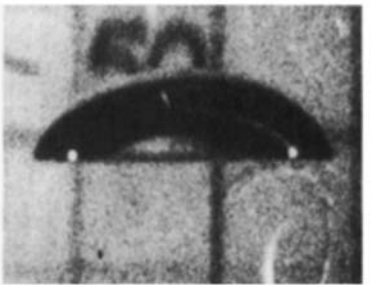
(f)


(g)


(h)

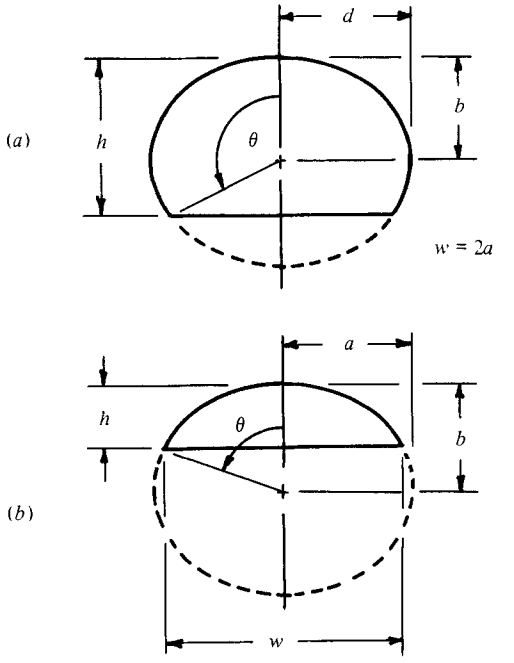

FIGURE 4. Parameters defining bubble shape: (*a*) ellipsoidal cap bubble with $\theta > 90°$; (*b*) ellipsoidal or spherical cap bubble with $\theta < 90°$.

other workers. The photographs of bubble shapes of Wairegi (1974), Angelino (1966) and Jones (1965) yield shape parameters in good agreement with the general correlation proposed in figures 5 and 6.

At intermediate R the bubbles have a significant indentation or dimple at the base. This indentation is a manifestation of the closed toroidal wake accompanying the bubble (Hnat & Buckmaster 1976). The wake circulates upward along the vertical axis of symmetry toward the base. The topmost point of the indentation is the forward stagnation point of the closed wake. The indentation is clearly visible in figure 3(*a*)-(*d*) where the upper surface of the indentation may be seen near the axis of the bubble. At the rim of the bubble the different refractive indices of the gas and the liquid prevent us from seeing how the indentation joins the outer surface of the bubble. Visual observation from below indicates a rounded lower edge, with the edge becoming sharper as R increases. These same refractive-index differences prevent the measurement of the exact location and radius of curvature of the indentation. The volume of

FIGURE 3. A 9·3 cm³ bubble in solutions with decreasing viscosity (grid in background is 2 × 2 cm).

	E	M	R	Shape
(*a*)	116	848	2·47	oblate ellipsoidal cap
(*b*)	116	266	3·57	oblate ellipsoidal cap
(*c*)	116	41·1	7·16	oblate ellipsoidal cap
(*d*)	116	5·51	13·3	oblate ellipsoidal cap
(*e*)	116	1·31	20·4	oblate ellipsoidal cap
(*f*)	116	0·103	42·2	oblate ellipsoidal cap
(*g*)	115	$4{\cdot}63 \times 10^{-3}$	94·0	spherical cap (closed wake)
(*h*)	114	$8{\cdot}60 \times 10^{-4}$	151	spherical cap (open wake)

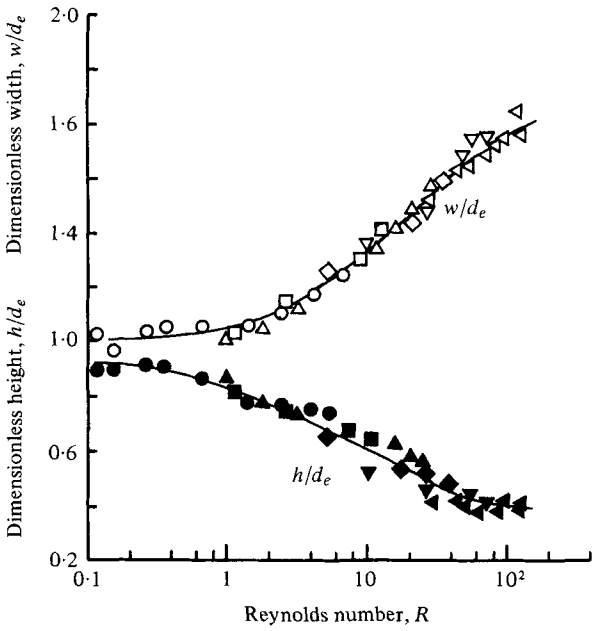

FIGURE 5. Dimensionless bubble height and width. Values of Morton numbers are: ○, 711; □, 55·5; △, 4·17; ◇, 1·03; ▽, 0·108; ◁, $5{\cdot}48 \times 10^{-3}$.

the indentation can be obtained by subtracting the bubble volume from the apparent volume calculated by assuming axial symmetry and using the shape parameters of figures 5 and 6. Indentation is first evident at $R \doteq 3$. The ratio of the volume of the indentation to the volume of the bubble increases to a plateau of about 0·4 at R between 20 and 60 and then decreases to essentially zero at $R \doteq 100$.

4. Bubble drag and rise velocity

Drag coefficients as a function of R are shown in figure 7. At low R the data approach the Hadamard–Rybczynski solution for creeping flow. The theory of Taylor & Acrivos agrees with the data up to $R \doteq 1$. For $R > 100$ the data approach $C_D \doteq 2{\cdot}7$, a value obtained for spherical caps by many workers. At intermediate R, between about 10 and 100, the drag coefficient may be a function of M. The transition from low- to high-M is evident in the positions of the data for the two lowest values, $M = 1{\cdot}64 \times 10^{-3}$ and $M = 5{\cdot}48 \times 10^{-3}$. We place the transition at $M = 4 \times 10^{-3}$. For larger values of M the relationship between C_D and R is independent of M. This result is in accord with the results on shape discussed above and suggests that for high-M liquids R is the only parameter required to describe the shape and the motion. For $M > 4 \times 10^{-3}$ the C_D–R relationship is well represented by

$$C_D = [(2{\cdot}67)^{0{\cdot}9} + (16/R)^{0{\cdot}9}]^{1/0{\cdot}9}. \tag{6}$$

The rise-velocity–volume relationship can be presented in a different way as suggested by Grace (1973). Figure 8 shows this alternative, R *versus* E with lines

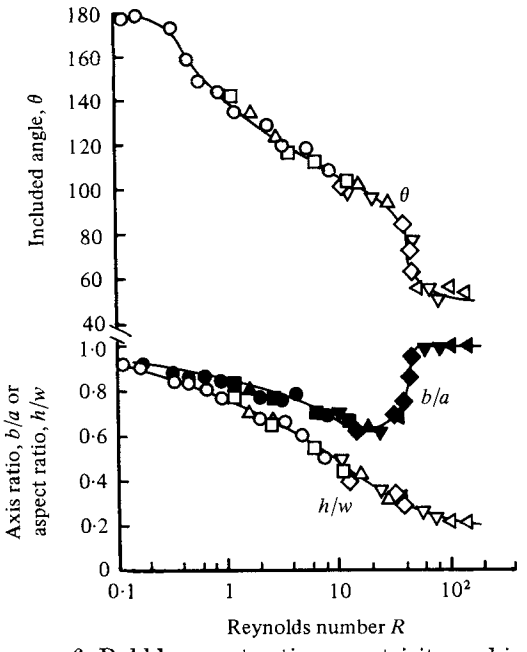

FIGURE 6. Bubble aspect ratio, eccentricity and included angle. For an explanation of the symbols see figure 5.

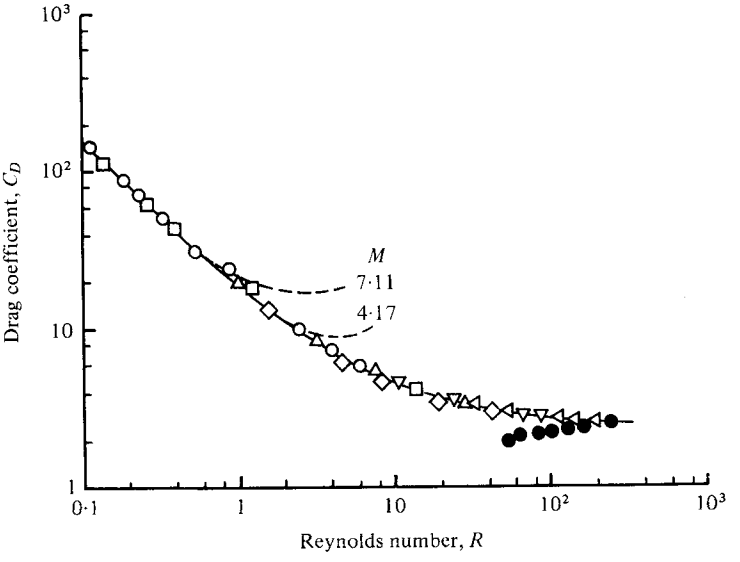

FIGURE 7. Drag-coefficient–Reynolds-number relationship: – – –, Taylor & Acrivos (1964); ——, equation (6). ●, $M = 1{\cdot}64 \times 10^{-3}$. For the other symbols see figure 5.

of constant M. A number of shape regimes are also shown on the plot. This figure differs from the original version in the location of the transition lines between regimes and the delineation of six additional shape regimes, namely: oblate ellipsoidal cap, wobbling disk-like ellipsoids, skirted bubbles with smooth skirts and with wavy skirts, and spherical caps with closed and open wakes.

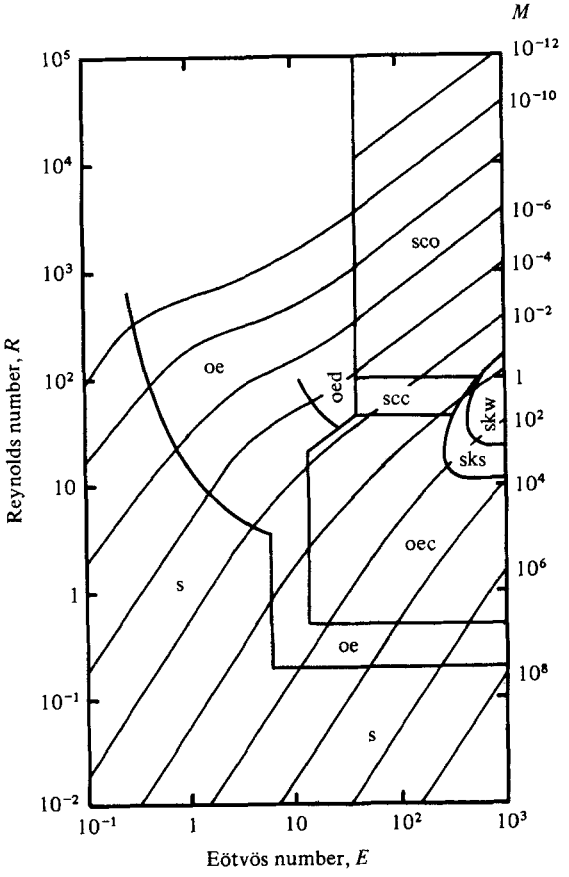

FIGURE 8. Shape regime map for bubbles in liquids: s, spherical; oe, oblate ellipsoid; oed, oblate ellipsoidal (disk-like and wobbling); oec, oblate ellipsoidal cap; scc, spherical cap with closed, steady wake; sco, spherical cap with open, unsteady wake; sks, skirted with smooth, steady skirt; skw, skirted with wavy, unsteady skirt.

The bubble rise velocities were compared with the expression of Wairegi & Grace (1976) derived for potential flow at the nose of an oblate ellipsoid:

$$U = \frac{\sin^{-1} e - e(1-e^2)^{\frac{1}{2}}}{e^3} (gb)^{\frac{1}{2}}, \tag{7}$$

where e, the eccentricity of the ellipsoid, is $(1-(b/a)^2)^{\frac{1}{2}}$, see figure 4. For a sphere ($e = 0$), equation (7) reduces to Davies & Taylor's (1950) result

$$U = \tfrac{2}{3}(gr_c)^{\frac{1}{2}}, \tag{8}$$

where r_c is the radius of the cap. Equation (8) agreed with the data within 5% for $R > 10$ if the radius of the cap were obtained by fitting a sphere over the front 75° ($\pm 37{\cdot}5°$ from the nose) segment as suggested by Collins (1966).

A very useful empirical correlation of the terminal rise velocity of large bubbles has been proposed by Angelino (1966):

$$U = KV^m, \tag{9}$$

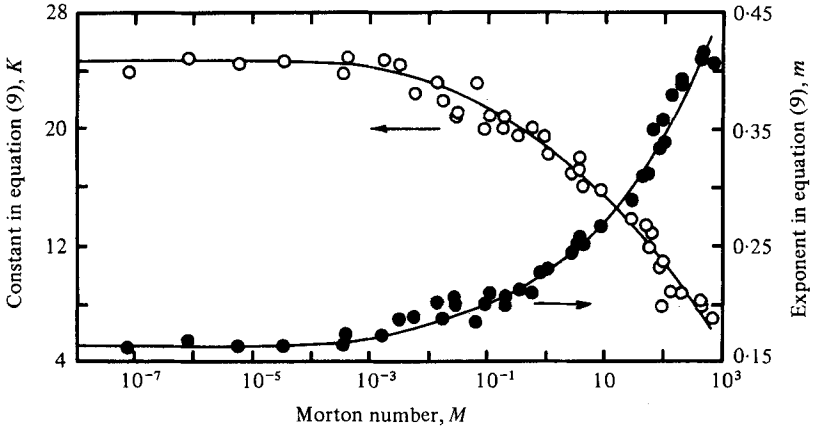

FIGURE 9. Parameters in terminal rise velocity correlation, equation (9): ○, K; ●, m.

where V is the bubble volume and K and m are parameters which depend upon the properties of the liquid. Figure 9 presents such a correlation of data from a large number of investigations. The criteria for data selection were $E > 40$ and $R \geqslant 2$. For low-M liquids the values of K and m are consistent with equation (8). A non-linear least squares fit to the data in figure 9 gave the following relationships with $E > 40$, $R > 2$:

$$K = 25/(1 + 0{\cdot}33M^{0{\cdot}29}), \tag{10}$$

$$m = 0{\cdot}167(1 + 0{\cdot}34M^{0{\cdot}24}). \tag{11}$$

The units of V and U are cm^3 and cm s^{-1}, respectively.

5. Bubble wakes and their geometry

The existence of a closed toroidal wake was demonstrated from the flow visualization with the H_2 tracers. Figure 10 and figure 11 (*a*, *b*, *c*) show closed toroidal wakes carried with all bubbles except the one with the highest Reynolds number. Only half of the wake is well visualized because of the cathode arrangement required to keep the bubble from splitting as discussed earlier. The circulation within the indentation is seen in figure 10 (*c*, *d*) where the tracer track disappears behind the rim of the bubble. The sequence of eight pictures given in figure 11 (*d*)–(*f*) and figure 12 (*a*)–(*e*) shows the wake development with increasing bubble volume in a solution with $M = 8{\cdot}2 \times 10^{-4}$. Figures 11 (*d*) and (*e*) show the same disk-like (aspect ratio of 0·25) ellipsoidal bubble with (*e*) taken 20 cm above (*d*). These bubbles wobble, but retain a closed wake. The two 'tails' shown in the first photograph disappear after the bubble rises some distance. The tails are from a line of tracer bubbles generated by the cathode before the bubble arrived. The wake remained closed throughout the bubble rise.

As bubble size increases, the wake volume increases until at $R \doteq 110$ the closed toroidal wake is replaced by an open, unsteady wake. The sharp transition from the closed to the open wake may not be observed with a stationary camera, see figures 12 (*b*, *c*). As R increases above 110 the wake becomes less ordered. The last photograph

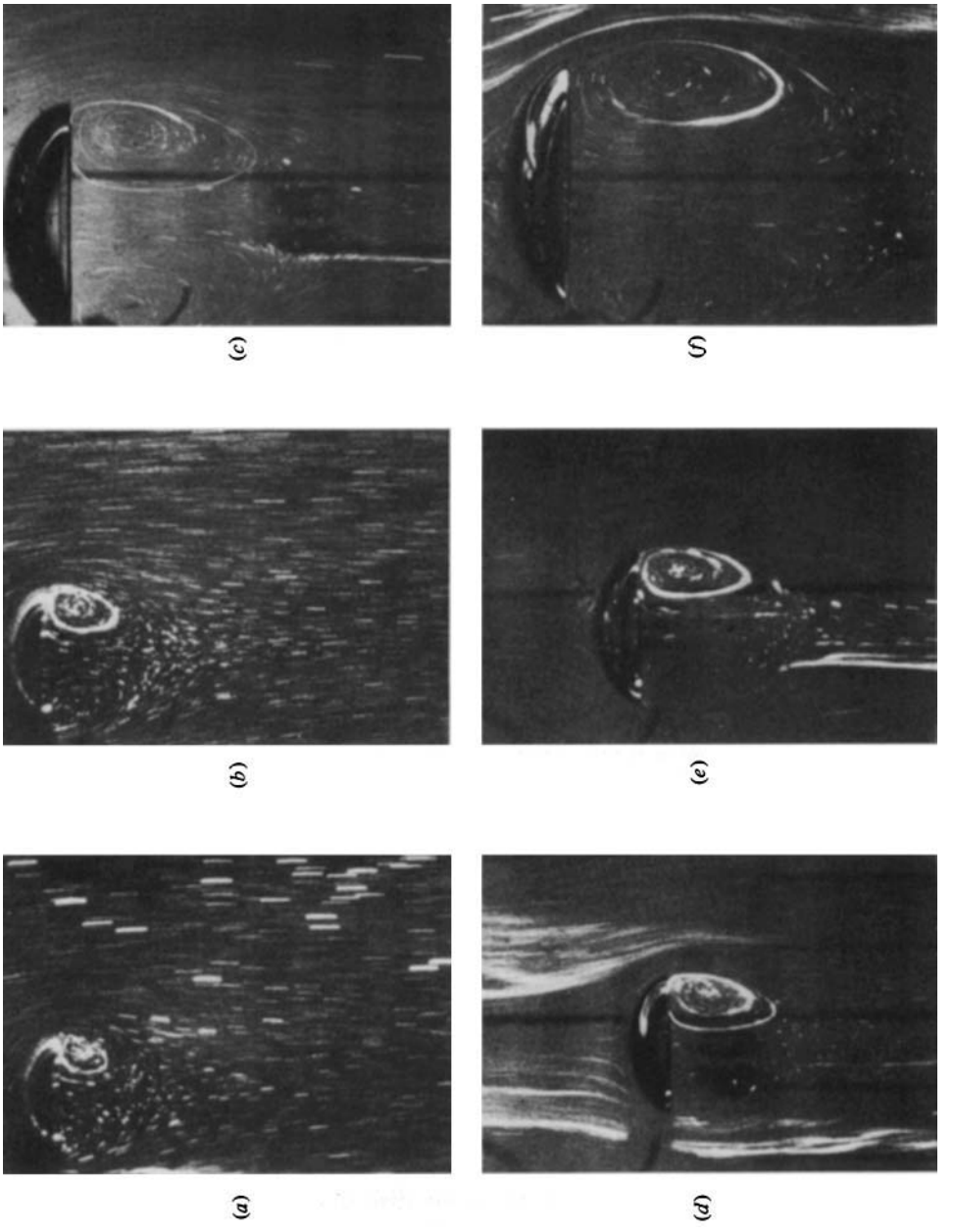

FIGURE 10. Bubble wake flow patterns (all bubbles shown at same magnification).

	E	M	R		E	M	R
(*a*)	96·2	0·962	18·2	(*d*)	95·6	0·144	32·1
(*b*)	116	0·962	22·0	(*e*)	151	0·144	37·4
(*c*)	202	0·962	39·6	(*f*)	240	0·144	67·4

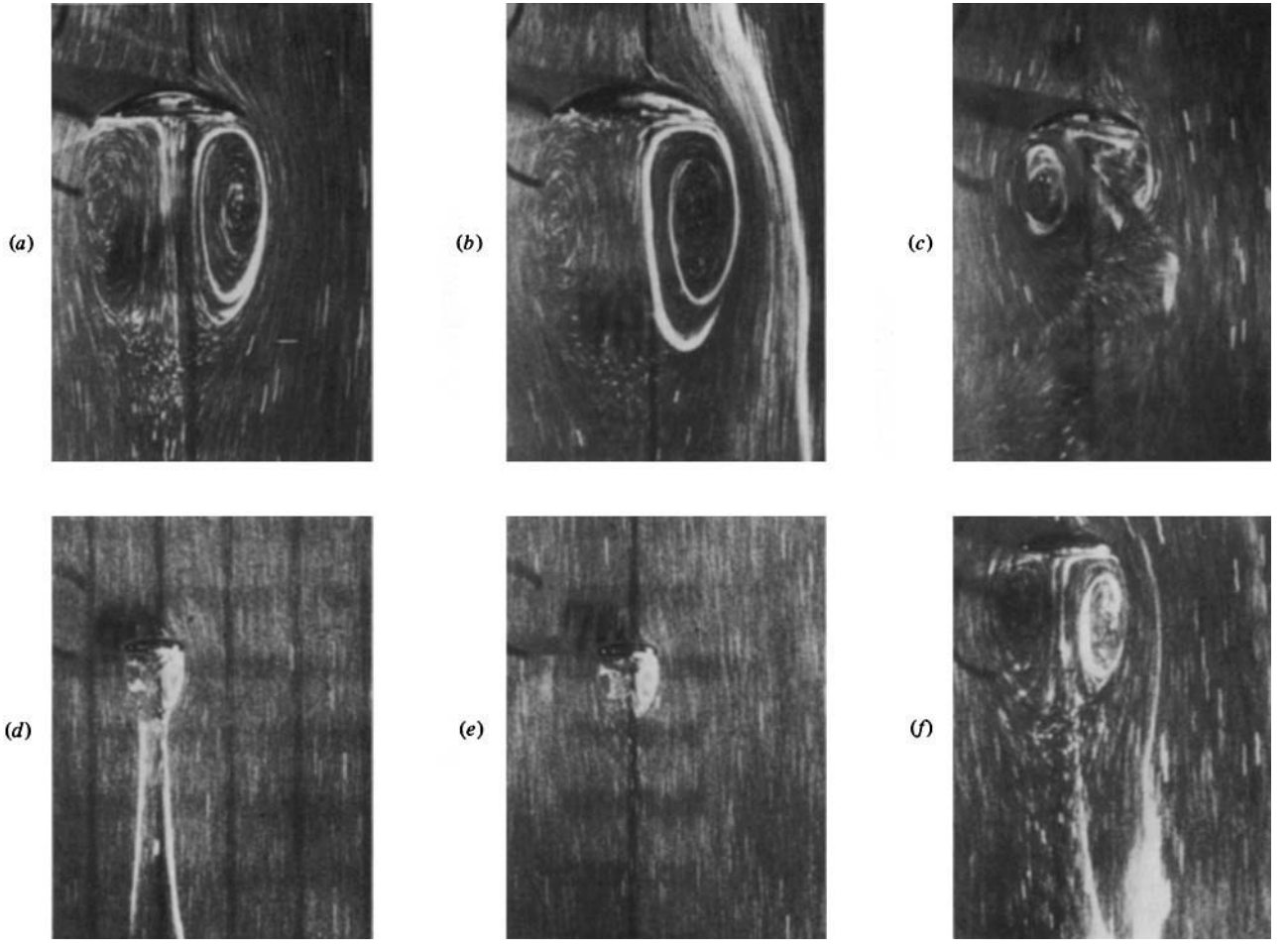

FIGURE. 11. (*a*, *b*, *c*) Bubble wake flow patterns. (*a*) and (*b*) at same magnification as figure 10; (*c*) at 62·4 % of this magnification. (*d*)–(*f*) Wake development with increasing bubble size.

	E	M	R		E	M	R
(*a*)	94·3	$4{\cdot}58\times10^{-3}$	77·9	(*d*, *e*)	21·2	$8{\cdot}20\times10^{-4}$	42·4
(*b*)	114	$4{\cdot}58\times10^{-3}$	91·6	(*f*)	51·1	$8{\cdot}20\times10^{-4}$	87·4
(*c*)	238	$4{\cdot}58\times10^{-3}$	159				

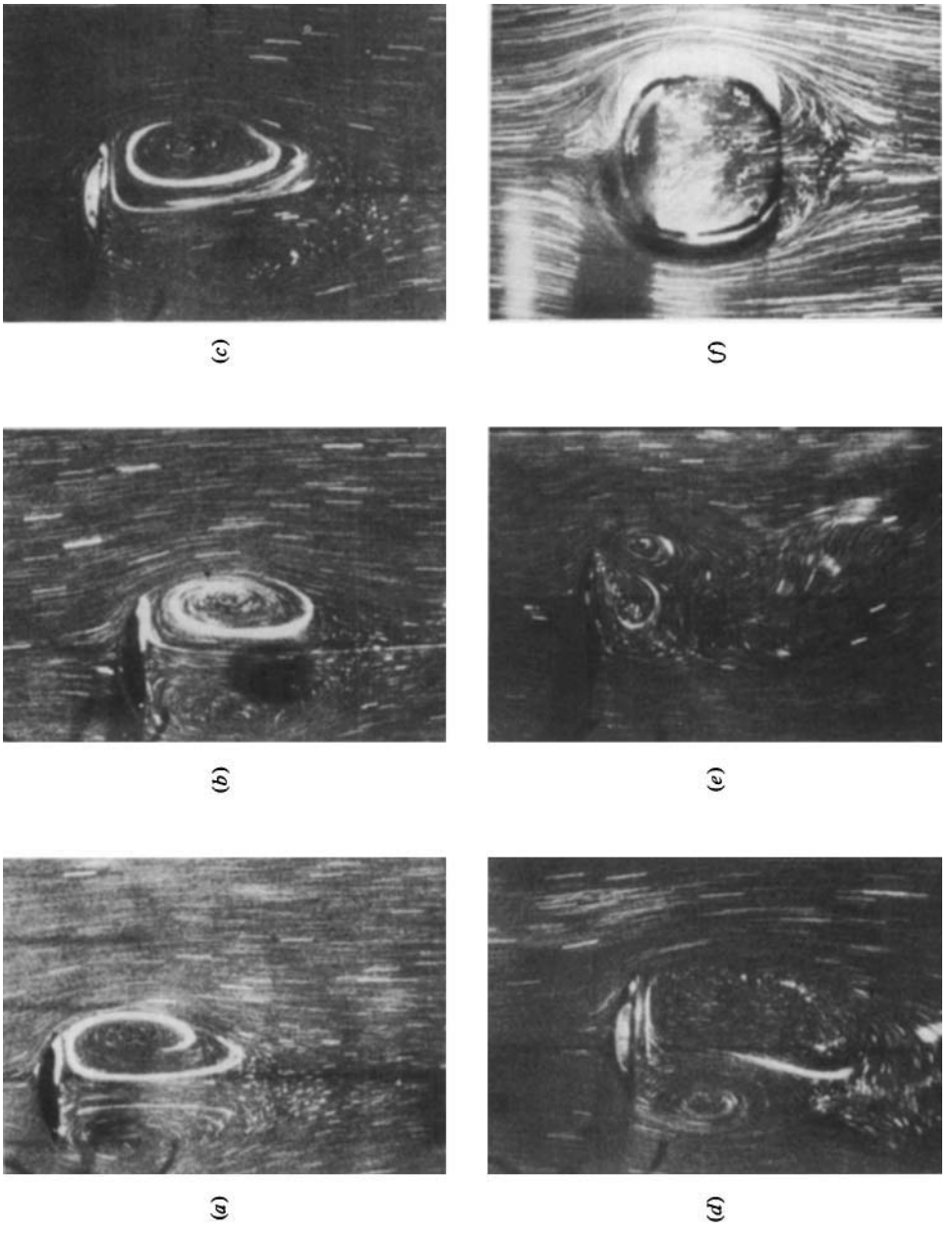

FIGURE 12. (a)–(e) Wake development with increasing bubble size; (f) skirted bubble.

	E	M	R		E	M	R
(a)	61·9	$8{\cdot}20\times10^{-4}$	99·5	(e)	237	$8{\cdot}20\times10^{-4}$	258
(b, c)	71·8	$8{\cdot}20\times10^{-4}$	110	(f)	292	26·7	22·1
(d)	81·2	$8{\cdot}20\times10^{-4}$	120				

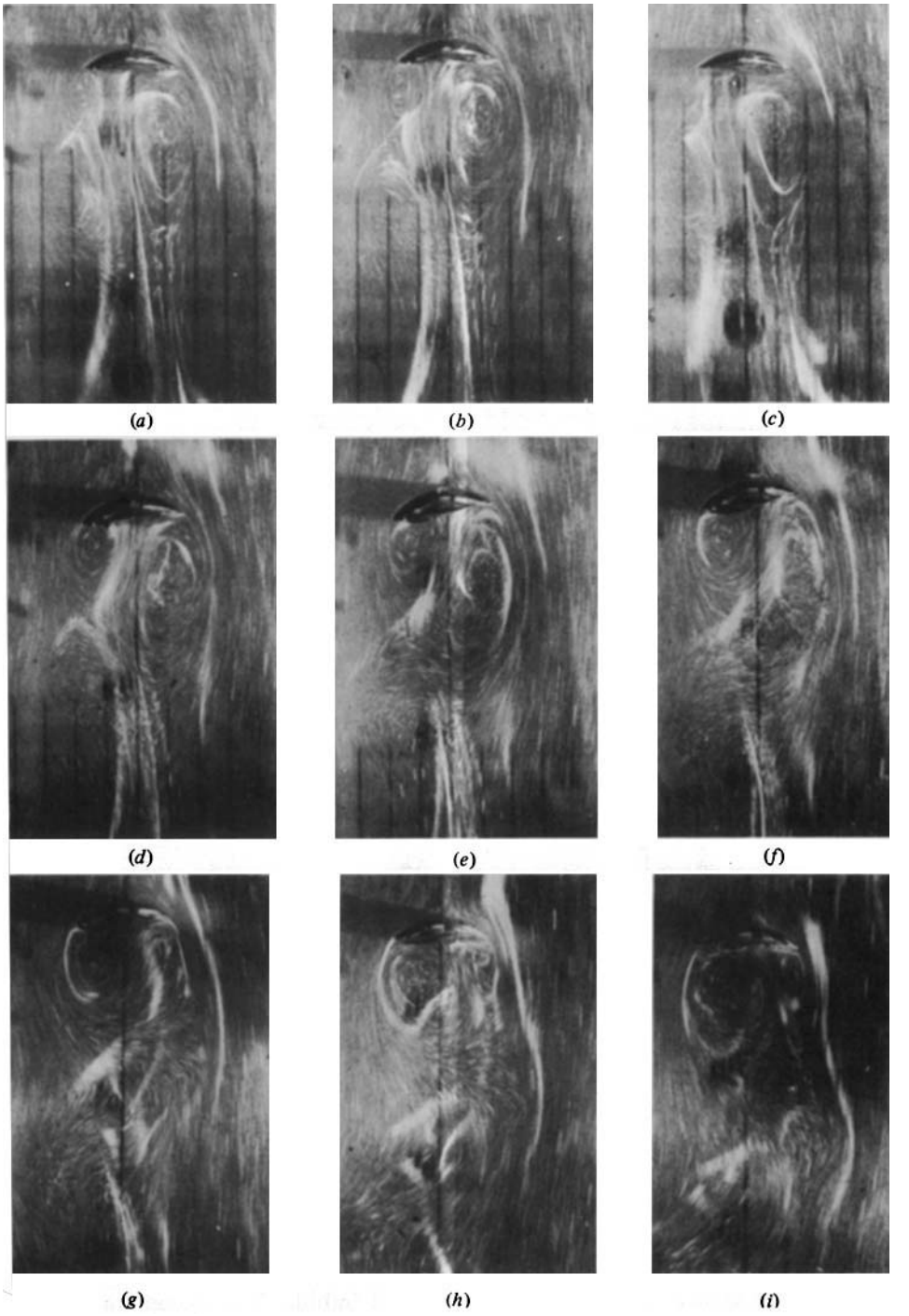

FIGURE 13. Open, unsteady wake behind a spherical cap bubble ($E = 210$) with $R = 146$ for $M = 4{\cdot}58 \times 10^{-3}$. Interval between successive photographs, 0·0417 s.

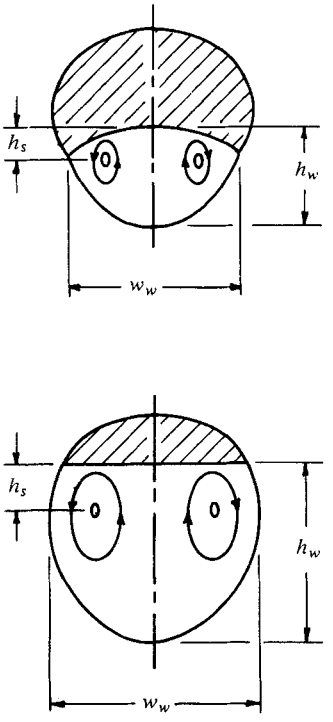

FIGURE 14. Parameters defining wake shape: (*a*) ellipsoidal cap bubble with $\theta > 90°$; (*b*) ellipsoidal or spherical cap bubble with $\theta < 90°$.

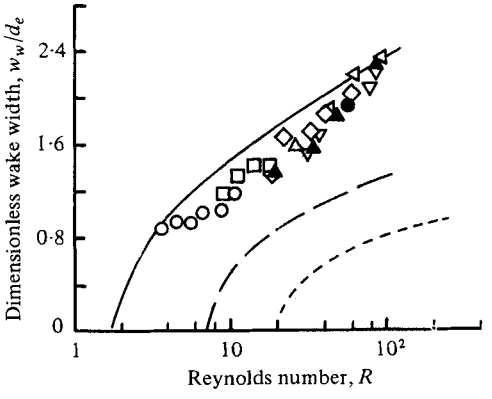

FIGURE 15. Dimensionless wake width: ——, solid spheres (Kalra & Uhlerr 1971); — —, rigid spheroid (aspect ratio 0·5); – – – –, rigid spheroid (aspect ratio 0·2). [Rigid spheroids from Masliyah (1972), Masliyah & Epstein (1970).] ●, Slaughter (1967), $M = 1{\cdot}73 \times 10^{-2}$; ▲, Hnat & Buckmaster (1976), $M = 6{\cdot}5 \times 10^{-2}$. Other symbols: ○, $M = 258$; □, $M = 43{\cdot}5$; △, $M = 4{\cdot}41$; ◇, $M = 0{\cdot}962$; ▽, $M = 0{\cdot}144$; ◁, $M = 4{\cdot}58 \times 10^{-3}$.

(*f*) of figure 12 shows the flow around a skirted bubble. The closed wake extends below the end of the skirt. The wake enclosed within the skirt is also circulating although the tracer tracks are distorted by refraction effects.

Figure 13 shows a sequence from a ciné film of the unsteady wake behind a bubble with $R = 146$. The bubble wobbles, but rises vertically, the wake is open and the

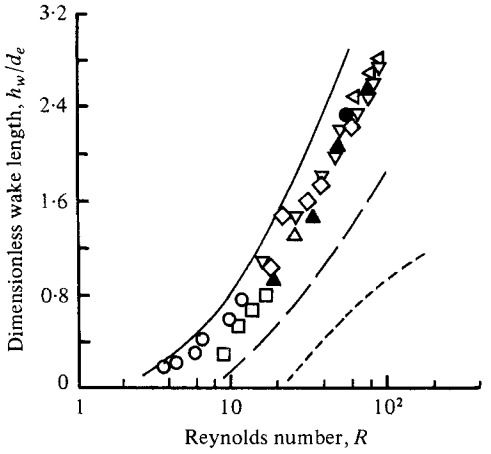

FIGURE 16. Dimensionless wake width. For an explanation of the symbols see figure 15.

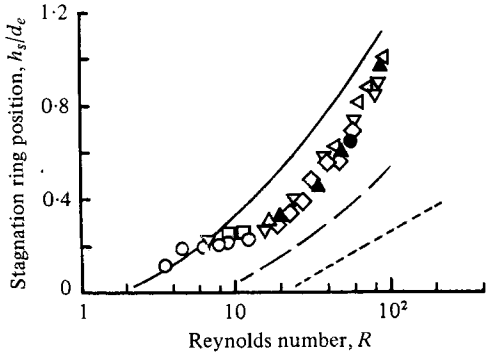

FIGURE 17. Dimensionless position of the wake stagnation ring. For an explanation of the symbols see figure 15.

base oscillates. Several determinations of the critical R for transition from a closed, steady wake to an open, unsteady wake were made for $2{\cdot}4 \times 10^{-4} \leqslant M \leqslant 5{\cdot}5 \times 10^{-3}$.† In all cases the transition occurred at $R = 110 \pm 2$. Since bubble shape and C_D are functions only of R for high-M liquids, the transition from closed to open wake is believed to occur at $R = 110$ for all high-M liquids. For low-M liquids, in which the shape depends upon one dimensionless group in addition to R, the transition Reynolds number may also depend upon another parameter, e.g. M or W. The scanty evidence available in the literature is consistent with the present finding. For example, Hnat & Buckmaster (1976) place the transition at $R \doteq 140$ while Coppus *et al.* (1977)‡ and Slaughter & Wraith (1968) show a closed wake at $R = 75$ and $R = 56$, respectively.

† Higher M liquids could not be used in the determination of the transition due to wall effects.

‡ The axis of the bubble wake in the photograph for $R = 75$ in this paper is not vertical. In their attempt to hold the bubble stationary by a downflow, they apparently did not achieve axisymmetry and the bubble 'wandered'.

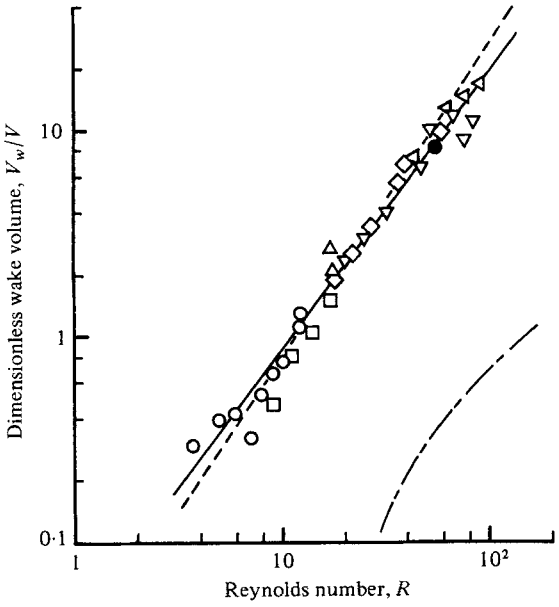

FIGURE 18. Dimensionless wake volume. — — — — —, rigid spherical caps (Kalra 1971); — – — – —, rigid spheres (Kalra & Uhlerr 1971). ●, Slaughter (1967), $M = 1{\cdot}73 \times 10^{-2}$. For the other symbols see figure 15.

Wake geometry

From projections of pictures similar to those shown in figures 10, 11 and 12 and from the streamlines shown below, the geometric parameters of the wake (see figure 14) were determined. The dimensionless wake width and length are shown as functions of R in figures 15 and 16. Also included as points are the data of Slaughter (1967) and Hnat & Buckmaster (1976). The continuous line represents data for solid spheres while the dashed lines represent numerical solutions for rigid spheroids with aspect ratios of 0·2 and 0·5. A similar plot of the location of the wake stagnation ring is shown in figure 17. The stagnation ring was in the horizontal plane of the maximum width of the wake. The distance from the axis of symmetry to the stagnation ring divided by the half-width of the wake, $w_W/2$, was 0·7 ($\pm$ 10 %); essentially identical with the value of 0·707 for the Hadamard and Hill spherical vortices.

The wake volume, V_W, calculated from the projected wake outline, is shown in dimensionless form in figure 18. Again good correlation with R alone is achieved and the data are well represented by

$$\frac{V_W}{V} = 0{\cdot}037R^{1{\cdot}4} \quad (3 < R < 110). \tag{12}$$

Also shown on the figure are lines representing the experimental data for rigid spheres and for rigid spherical caps. The bubbles carry much more fluid with them than rigid spheres due to the deformation from spherical shape. The dotted line represents the data for rigid spherical caps (Kalra 1971). This line gives the dimensionless wake volume for a rigid spherical cap having the same aspect ratio (height/width) as a

bubble at the same R. The values necessary to plot this curve were obtained by cross-plotting the original data of Kalra. The good agreement between the present data and those for spherical caps reflects the fact that the locus of separation is at the rim in each case.

6. Streamlines and velocities around rising bubbles

Streamlines of the flow around rising bubbles traced from ciné films are presented in the series of figures to follow. Since the camera was moving upward, the bubble appears stationary with a vertical downflow of fluid. In all figures the positions of the tracers external to the wake have been connected by smooth curves.

The accuracy of the experimental streamlines was checked by measurements around a spherical bubble at $R = 0{\cdot}087$ and around slightly deformed bubbles with $R < 0{\cdot}5$ and $W < 1$. In the former case good agreement was found with the streamlines and velocities of the Hadamard–Rybczynski solution for creeping flow around a gas bubble; see figure 21 and the discussion below. In the latter case ($R < 0{\cdot}5$, $W < 1$) good agreement was found with the streamlines of Taylor & Acrivos (1964) for deformed bubbles.

Figures 19(*a*)–(*d*) display streamlines for the 9·3 cm^3 bubble of figure 3 in four solutions with M decreasing from 848 to $4{\cdot}63 \times 10^{-3}$. All bubbles have closed toroidal wakes.†

General features of the flow

No fluid is exchanged between the toroidal wake and the external flow for $R < 110$ and $M > 4 \times 10^{-3}$. Within the wake the tracer bubbles disappear into the indentation and then reappear for another identical trip around the stagnation ring. The liquid velocity within the closed wake is much less than the bubble rise velocity. For ellipsoidal cap bubbles the boundary of the closed wake does not coincide with the boundary of the ellipsoid which fits the frontal surface of the bubble except at $R \doteq 5$. For $R > 5$ the wake is larger than the frontal ellipsoid; it is elongated in the vertical direction; for $R < 5$ the reverse occurs, see figures 19(*a*, *b*). For spherical cap bubbles ($R > 45$) the wake is longer than the frontal sphere for $R \gtrsim 50$, see figure 19(*d*). For these bubbles the wake is far from spherical although at higher Reynolds numbers it more nearly approaches this shape.

The external flow ahead of the bubble is not slowed appreciably as it approaches; however, after passing the base of the bubble the velocity decreases due to the larger shear stress at the wake boundary compared to that at the front surface of the bubble. There is no fore–aft symmetry even for bubbles whose wakes coincide with the frontal ellipse. Velocities behind the bubble are appreciably lower than ahead of the bubble. When a bubble passes a stationary observer, he would see appreciable drift, i.e. the bubble moves a large volume of the surrounding fluid upward as it passes the observation point. For $R > 110$, where the wake is unsteady, the flow ahead of the bubble and up to the average position of the base is little affected by the open wake. Below

† Copies of the following diagrams of streamlines for flow around bubbles can be obtained on request from M. E. Weber: (1) oblate ellipsoidal cap bubbles with $M = 266$ for $R = 4{\cdot}5$ and $R = 10{\cdot}1$; (2) spherical cap bubbles with $M = 4{\cdot}63 \times 10^{-3}$ for $R = 45{\cdot}5$ and $R = 60{\cdot}9$; (3) two bubbles with $M = 5{\cdot}51$ for $R = 28{\cdot}9$, one just below and one just above the critical size required for skirt formation.

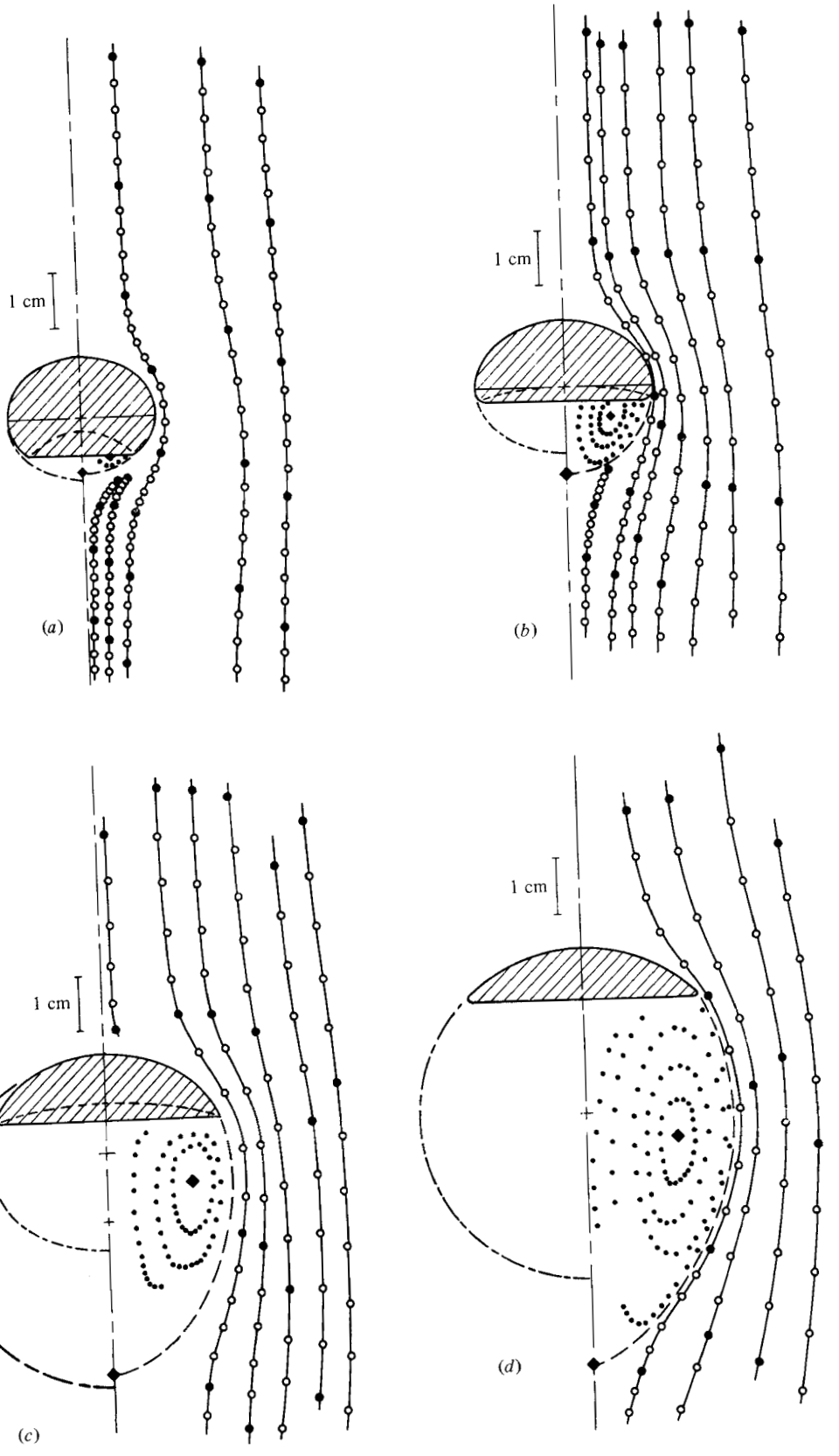
1 cm
(a)
1 cm
(b)
1 cm
(c)
1 cm
(d)

the oscillating base the flow is clearly unsteady and the tracer paths observed at different times may cross.

The presence of a skirt occasions surprisingly little change in the external flow field. The terminal rise velocity is essentially the same with or without a skirt, a fact noted by others (e.g. Wairegi & Grace 1976). Although there is a slight widening of the bubble, the skirt essentially encloses a portion of the toroidal wake which exists for a bubble just below the critical size. The closed toroidal wake extends somewhat beyond the lower edge of the skirt and there is a toroidal circulation in the liquid enclosed by the skirt. However, the rate of circulation is decreased in the presence of the skirt.

7. Discussion

No complete theoretical treatment of the fluid mechanics of non-spherical bubbles exists for $R > 1$. In this section we make a few comparisons between our data and model flows.

Wake velocities

Velocities within the closed wake were measured at the horizontal plane containing the stagnation ring. This plane is at the maximum width of the wake and the wake velocities, u_{we}, are vertical. Data for a spherical cap bubble with $R = 94$ in a solution with $M = 4{\cdot}63 \times 10^{-3}$ (see figure 19*d*) are shown in figure 20. The points, which were obtained from five different bubbles of the same size, indicate the reproducibility of the data. The horizontal distance from the axis of symmetry is made dimensionless with the half-width of the wake. Also plotted are curves from four models of a spherical vortex: Hill's vortex (external potential flow), the boundary-layer corrections to Hill's vortex of Harper & Moore (1968) and of Parlange (1970) and Hadamard's creeping flow vortex; the last three having equal external and internal viscosity. The data are well fitted by the Harper & Moore theory even though the wake is not spherical and the bubble covers part of the wake surface. Hence the assumption of Harper & Moore (1968), that the fluid within the spherical vortex moving from the region of the rear stagnation point to the region of the front stagnation point retains its vorticity, is more reasonable than the vorticity destruction assumption of Parlange (1970). Additional data show that the dimensionless wake velocity decreases toward the Hadamard prediction as R decreases.

External velocities

Velocities in the solution at the horizontal plane of the maximum bubble width were measured for a spherical bubble and the ellipsoidal cap bubbles of figures 3 and 19.

FIGURE 19. Tracer paths for a 9·3 cm³ ellipsoid cap bubble: (*a*) for $M = 848$ and $R = 2{\cdot}47$ ($E = 116$), time between successive frames 0·0286 s (within wake, every fifth frame); (*b*) for $M = 5{\cdot}51$ and $R = 13{\cdot}3$ ($E = 116$), time between successive frames 0·0286 s (within wake, every second frame); (*c*) for $M = 0{\cdot}103$ and $R = 42{\cdot}2$ ($E = 116$), time between successive frames 0·0291 s; (*d*) for $M = 4{\cdot}63 \times 10^{-3}$ and $R = 94{\cdot}0$ ($E = 115$), time between successive frames 0·0298 s. ○, position of tracer external to wake in every frame; ●, position of tracer external to wake in every fifth frame; ●, position of tracer within the closed wake; — - — -, boundary of sphere or ellipsoid which fits the frontal surface of the bubble; — — — —, boundary of closed wake; ◆, position of wake rear stagnation point and wake stagnation ring.

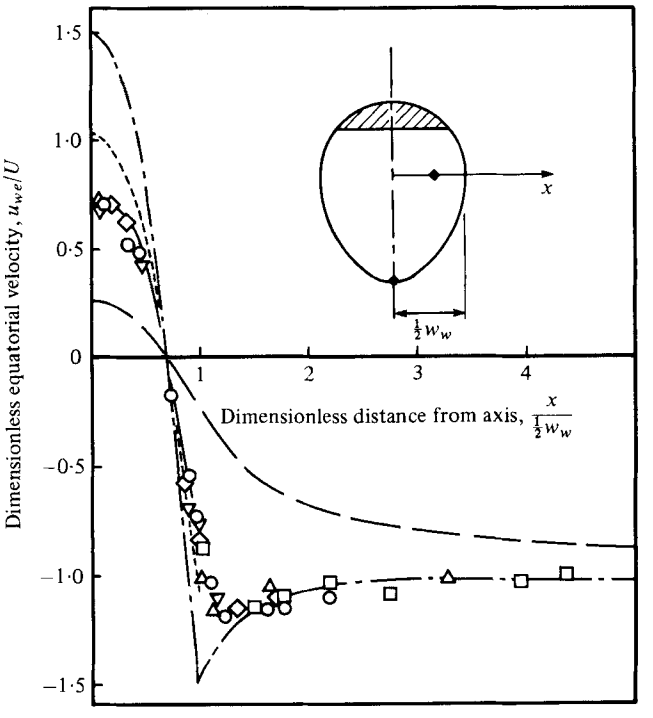

FIGURE 20. Dimensionless wake velocity in the plane of the wake stagnation ring for a spherical cap bubble with $R = 94{\cdot}0$ for $M = 4{\cdot}63 \times 10^{-3}$. — — —, Hill's spherical vortex; – – – – –, Parlange (1970) model; ——, Harper & Moore (1968) model; — — — —, Hadamard creeping-flow vortex with equal external and internal viscosities.

These velocities, $u_{\theta e}$, are presented in dimensionless form in figure 21. The horizontal distance was made dimensionless with the semi-major axis of the ellipse and the radius of the sphere. Also shown in the figure is a curve for creeping flow around a spherical bubble and a shaded region for potential flow around ellipses. The data for the spherical bubble at $R = 0{\cdot}087$ are in excellent agreement with the creeping flow solution. For the ellipsoidal cap bubble the velocities some distance from the bubble surface approach the potential flow velocity as R increases. However, the boundary layer adjacent to the bubble surface is clearly evident at dimensionless distances $< 1{\cdot}5$. At the larger values of R there is a local maximum in the velocity, which then approaches the free-stream velocity from above. A similar velocity maximum has been reported by Seeley, Hummel & Smith (1975) for solid spheres at $R \gtrsim 290$.

Since no solutions are available for the velocity field around ellipsoidal and spherical cap bubbles at $R < 110$, the tracer trajectories were compared with potential flow streamlines for spheroids. The agreement was good ahead of the plane of maximum bubble width for $R > 2$ at distances from the bubble surface larger than one major semiaxis. Figure 21 illustrates this for the equatorial plane. Below this plane, i.e. behind the bubble, agreement was poor.

For larger R the velocities in the liquid near a rising bubble have been derived by Moore (1963) through a boundary-layer correction to potential flow around a sphere. This is the only theoretical solution presently available for $R > 1$. An experimental

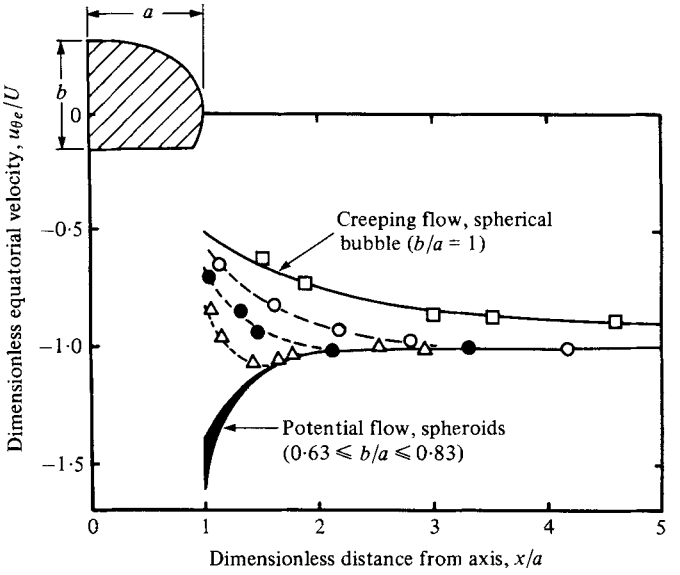

FIGURE 21. Equatorial velocities in the continuous phase for a spherical bubble (□, R = 0·087, b/a = 1·0) and for ellipsoidal cap bubbles (○, R = 2·47, b/a = 0·83; ●, R = 13·5, b/a = 0·73; △, R = 42·2, b/a = 0·81).

tracer trajectory near the surface of a spherical cap bubble is shown in figure 22. Also shown are the positions of the tracer as predicted by potential flow and by Moore's boundary-layer theory. These calculations were begun from the topmost tracer position in the figure and the tracer positions predicted by assuming that the tracer follows the fluid motion exactly. There is good agreement between the boundary-layer treatment and the data up to the rim of the bubble even though this bubble has an open wake and an oscillating base.

8. Conclusions

The present results show that for liquids with high Morton number, $M > 4 \times 10^{-3}$, dimensionless bubble and wake shapes are functions only of Reynolds number, as is the drag coefficient. A number of shape regimes have been delineated and shown on the regime map of Grace (1973). Terminal rise velocities have been correlated with bubble volume for $E > 40$, $R > 2$. In high-M liquids bubbles trail closed toroidal wakes for $R < 110$. The wakes are larger than the frontal spheroid or sphere for $R > 5$.

Streamlines within the wake and external to the bubble and its wake were determined using the hydrogen bubble tracer technique. At the present time we can predict the flow field around a bubble only for $R < 1$. If we confine our attention to the region forward of the base of the bubble, potential flow and the boundary-layer correction provide reasonable predictions for spherical-cap bubbles. No predictions have yet been made for the flow field behind spherical-cap bubbles with closed wakes ($45 < R < 110$) or for any portion of the flow field for ellipsoidal cap bubbles ($1 < R < 45$). Our data provide a test and a challenge for future theoretical and numerical work.

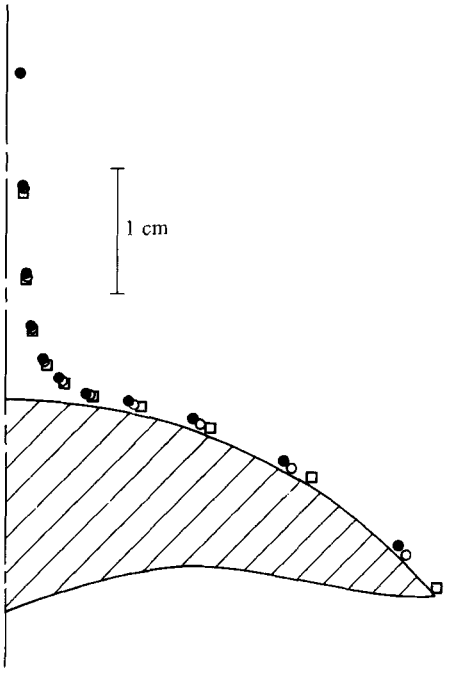

FIGURE 22. Tracer path near the surface of a spherical cap bubble (E = 237) with R = 265 for $M = 7{\cdot}40 \times 10^{-4}$. Time between successive frames 0·0286 s. ●, tracer position; □, potential flow prediction; ○, Moore (1963) boundary-layer prediction.

This work was supported by the Natural Sciences and Engineering Research Council of Canada.

REFERENCES

ANGELINO, H. 1966 Hydrodynamique des grosses bulles dans les liquides visqueux. *Chem. Eng. Sci.* **21**, 541–550.

BHAGA, D. 1976 Bubbles in viscous liquids: shapes, wakes and velocities. Ph.D. thesis, McGill University, Montreal.

CLIFT, R. C., GRACE, J. R. & WEBER, M. E. 1978 *Bubbles, Drops and Particles.* Academic.

COLLINS, R. 1966 A second approximation for the velocity of a large bubble rising in an infinite liquid. *J. Fluid Mech.* **25**, 469–480.

COPPUS, J. H. C., RIETEMA, K. & OTTENGRAF, S. P. P. 1977 Wake phenomena behind spherical-cap bubbles and solid spherical-cap bodies. *Trans. Inst. Chem. Eng.* **55**, 122–129.

DAVIES, R. M. & TAYLOR, G. I. 1950 The mechanics of large bubbles rising through extended liquids and through liquids in tubes. *Proc. Roy. Soc.* A **200**, 375–590.

GRACE, J. R. 1973 Shapes and velocities of bubbles rising in infinite liquids. *Trans. Inst. Chem. Eng.* **51**, 116–120.

GUTHRIE, R. I. L. & BRADSHAW, A. V. 1969 The stability of gas envelopes trailed behind large spherical cap bubbles rising through viscous liquids. *Chem. Eng. Sci.* **24**, 913–917.

HARPER, J. F. 1972 The motion of bubbles and drops through liquids. *Adv. Appl. Mech.* **12**, 59–129.

HARPER, J. F. & MOORE, D. W. 1968 The motion of a spherical liquid drop at high Reynolds number. *J. Fluid Mech.* **32**, 367–391.

HNAT, J. G. & BUCKMASTER, J. D. 1976 Spherical cap bubbles and skirt formation. *Phys. Fluids* **19**, 182–194. Erratum. *Ibid.* **19**, 611.

JONES, D. R. M. 1965 The steady rise of air bubbles in viscous liquids. Ph.D. thesis, University of Cambridge.

KALRA, T. R. 1971 Bluff body wakes - geometry and mass transfer. Ph.D. thesis, Monash University, Melbourne.

KALRA, T. R. & UHLERR, P. H. T. 1971 Properties of bluff-body wakes. *4th Australian Conf. Hydraulics and Fluid Mech., Melbourne.*

MASLIYAH, J. B. 1972 Steady wakes behind oblate spheroids: flow visualization. *Phys. Fluids* **15**, 1144–1146.

MASLIYAH, J. B. & EPSTEIN, N. 1970 Numerical study of flow past spheroids. *J. Fluid Mech.* **44**, 493–512.

MOORE, D. W. 1963 The boundary layer on a spherical bubble. *J. Fluid Mech.* **16**, 161–176.

PARLANGE, J.-Y. 1969 Spherical-cap bubbles with laminar wakes. *J. Fluid Mech.* **37**, 257–263.

PARLANGE, J.-Y. 1970 Motion of spherical drops at large Reynolds numbers. *Acta Mech.* **9**, 323–328.

SCHRAUB, F. A., KLINE, S. J., HENRY, J., RUNSTADLER, P. W. & LITTELL, A. 1965 Use of hydrogen bubbles for quantitative determination of time-dependent velocity fields in low-speed water flows. *Trans. A.S.M.E.* D, *J. Basic Engng* **87**, 429–444.

SEELEY, L. E., HUMMEL, R. L. & SMITH, J. W. 1975 Experimental velocity profiles in laminar flow around spheres at intermediate Reynolds numbers. *J. Fluid Mech.* **68**, 591–608.

SLAUGHTER, I. 1967 The motion of gas bubbles rising singly and in streams through liquids. Ph.D. thesis, University of Newcastle upon Tyne.

SLAUGHTER, I. & WRAITH, A. E. 1968 The wake of a large gas bubble. *Chem. Eng. Sci.* **23**, 932.

TADAKI, T. & MAEDA, S. 1961 On the shape and velocity of single air bubbles rising in various liquids. *Kagaku-Kogaku* **25**, 254–264.

TAYLOR, T. D. & ACRIVOS, A. 1964 On the deformation and drag of a falling viscous drop at low Reynolds number. *J. Fluid Mech.* **18**, 466–477.

WAIREGI, T. 1974 The mechanics of large drops and bubbles moving through extended liquid media. Ph.D. thesis, McGill University, Montreal.

WAIREGI, T. & GRACE, J. R. 1976 The behaviour of large drops in immiscible liquids. *Int. J. Multiphase Flow* **3**, 67–77.